Chapter 2

# Landslides Triggered by Typhoon Morakot in Taiwan

Ssu-Yao Yang, Chyan-Deng Jan and Ji-Shang Wang

Additional information is available at the end of the chapter

http://dx.doi.org/10.5772/intechopen.76930

**Abstract**

Landslides are general geomorphic erosion processes on hillslopes and can usually cause severe threats to human life and property due to their unexpected occurrence and fast traveling. Typhoon Morakot (in 2009) released more than 2000 mm rainfall during 6 days at the beginning of August 5 in Taiwan, leading to a large number of landslides, especially in southern Taiwan. Here we significantly devote this chapter to address the causes and effects of landslides in Cishan River watershed accompanied with the primary factors of landslide triggering such as the geologic and topographic settings and rainfall characteristics. We evaluate the devastation of landslides caused by Typhoon Morakot and its aftermath, and also assess the present status of landslide hazards mitigation strategies in Taiwan.

**Keywords:** landslide, river channel adjustment, Taiwan, Typhoon Morakot

## 1. Introduction

Landslides are general geomorphic erosion processes on hillslopes and can usually cause severe threats to human life and property due to their unexpected occurrence and fast traveling. Landslides can mobilize a cascades of loose materials from hillslopes into river channels, affecting the sediment yield of watersheds and its corresponding consequent evolution of river channels, habitats, deltas and coast lines in the downstream. Typically, this geomorphic erosion (i.e., landslides) occurs in mountainous landscapes with strong ground motion from earthquakes [1], snow-melt infiltration [2], and rainfall infiltration [3, 4].

Taiwan is an island of an area of 36,000 km$^2$, and two-thirds of its area are covered by rugged mountains and hills, steep topography, young (3 million years) and weak geological formulations, active earthquakes, and loose soils [5]. Earthquakes and heavy rains play a major role on contributing to the occurrence of landslides. Many landslides have been mainly triggered

by typhoons that usually brought heavy rains in Taiwan. In recently decades, the most severe landslides triggered by heavy rains in Taiwan are those by Typhoon Morakot in the period of August 5 to 10, 2009. Typhoon Morakot brought more than 2000 mm rainfall during 6 days, leading to a large number of landslides, especially in southern Taiwan. The understanding of landslide hazards has been still limited until Typhoon Morakot hit in Taiwan that caused a total of 45,125 of landslides and the catastrophic Hsiaolin landslide in the Cishan River watershed (CRW). The Hsiaolin landslide generated a huge debris dam that blocked the Cishan River and its consequent dam break caused more than 400 people dead and missing; also, the village itself no longer exists [44].

After Typhoon Morakot, the natural environmental conditions of watershed systems were significantly changed due to severe landslides and associated damages. For developing cost-effective landslide hazards mitigation strategies and measures, we should have better understanding on the causes and effects of landslides. Basing on the data taken from the study area of CRW, we devote this chapter to: (1) address the causes and effects of landslides in this watershed (i.e., CRW) accompanied with the primary factors of landslide triggering such as the geologic and topographic settings and rainfall characteristics; (2) evaluate the devastation of landslides caused by Typhoon Morakot and its aftermath; (3) assess the present status of landslide hazards mitigation strategies in Taiwan. Results from landslide research in this chapter lays the foundation and establishes the guidelines for developing possible effective landslide hazards mitigation strategies and measures.

## 2. General information of landslide triggers in Cishan River watershed, Taiwan

The island of Taiwan is located at the obliquely convergent boundary of the Eurasian continent and the Philippine Sea plate and separated from Eurasia continent by the 175 km wide Taiwan Strait. This collision of the Luzon arc results in two-thirds of its area being covered by rugged mountains and hills, steep topography, young (3 million years) and weak geological formulations, active earthquakes, and loose soils [5]. The average elevation is 765 m and about 31% of the total island area has an elevation of exceeding 1000 m. Most mountains are very steep with slope gradients of 25° and local relief of 1000 m or more.

Taiwan is periodically disturbed by typhoons and local storms and experiences a 2500 mm mean annual rainfall depth equivalent to a triple of global mean values. Majority of rainfall occurs between June and October when trade wind and typhoons strongly provide the sources of moisture. During the rainy seasons, the geological and climatic regimes usually combine to generate severe hillslope denudation by soil erosion, landslides, and debris flows.

Dadson et al. [6] indicates that the rivers of Taiwan transfer suspended sediment of 384 Mt/y to the ocean based on the data measured between 1970 and 1999. This represents 1.9% of estimated global river-borne suspended-sediment discharges but is only derived form 0.024% of Earth's subaerial surface. The Erosion rate were quite high in the eastern Central Range and southwestern region of Taiwan, especially on the Western Foothills with a rate of up to 60 mm/y [6].

### 2.1. Cishan River watershed and its lithologic complexes

Cishan River watershed lies on the Western Foothills of Taiwan and has an area of 842 km$^2$ and a mean gradient of 39.3%. Its maximum elevation of 3950 m is near the Southwestern Foothills of Jade Mountain, gradually decreasing from north to south to 31 m, with mean elevation of 473 m. Obviously, there is a significant difference between the maximum and minimum elevations in this long, narrow watershed (**Figure 1**). The geologic setting is underlain by sandstone, shale, slate, and phyllite, and drains geological ages between Eocene to Pleistocene distributed from the upper to lower regions. This is clear that the geological formation is young and weak (between 5.3 and 0.01 million years ago), leading to poorly lithologic resistance to erosion. The Cishan River is 118 km in length, flowing through the watershed. The geomorphic characteristics (i.e., elevation and slope) were obtained by digitizing a 5 × 5 m digital elevation model (provided by Water Resources Agency, Taiwan, WRA) using Geographic Information System (GIS).

**Figure 2** shows a geological map of CRW (provided by the Geological Survey Center, MOEA, Taiwan). There are nine lithologic complexes and rock units in the Cishan River watershed:

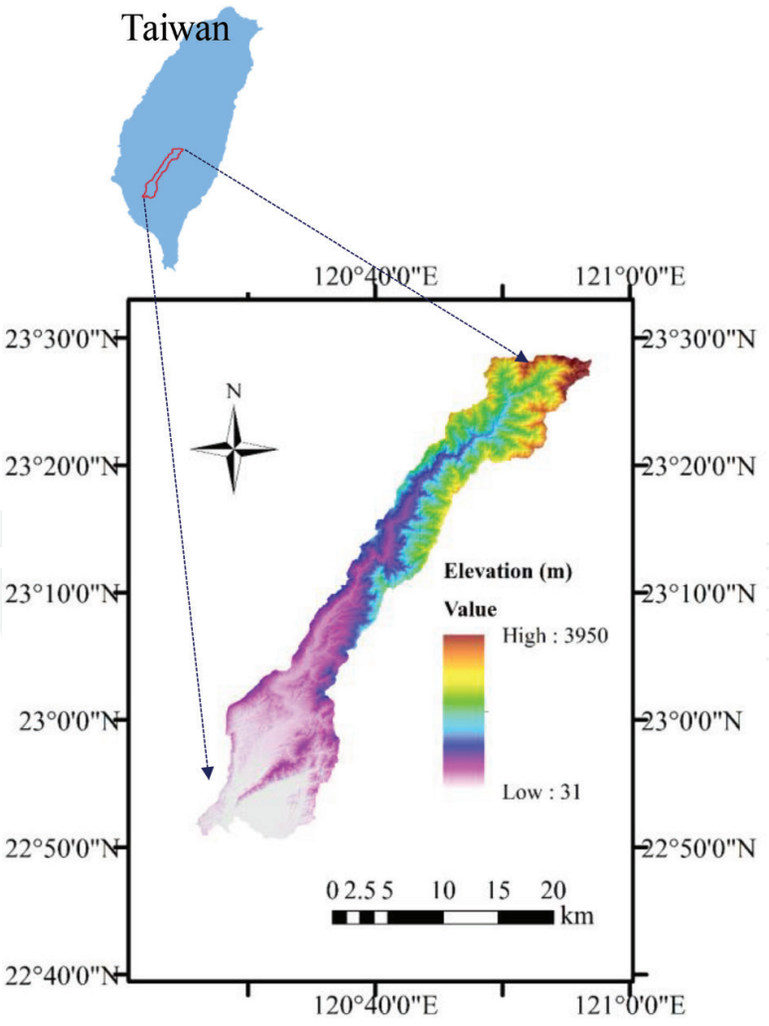


**Figure 1.** Locations and topography of Cishan River watershed (CRW).

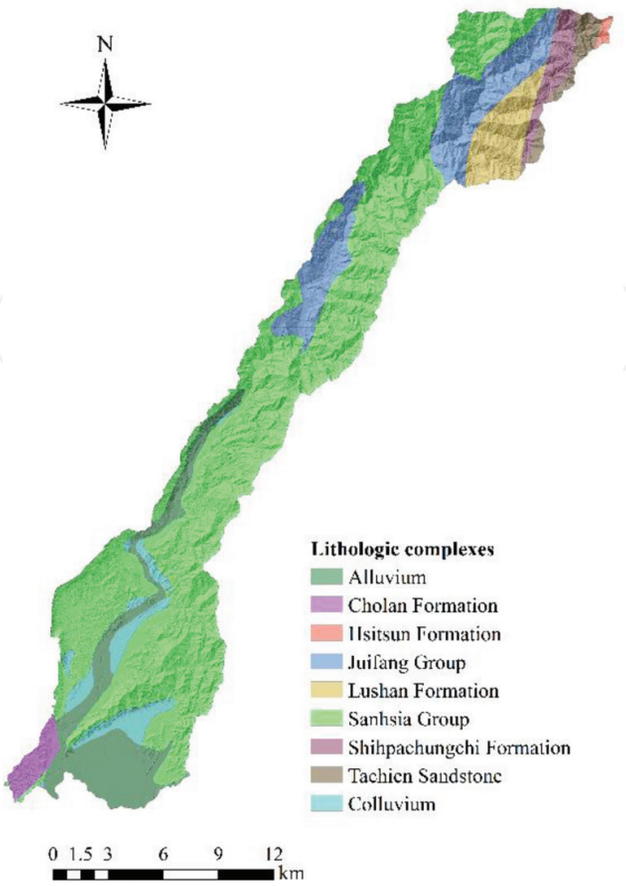


**Figure 2.** Map of lithologic complexes for the Cishan River watershed.

(a) Cholan Formation, Pliocene in age, (b) Hsitsun Formation, Eocene to Oligocene, (c) Juifang Group, Middle Miocene, (d) Lushan Formation, Miocene in age, (e) Sanhsia Formation, Late Miocene to Pliocene, (f) Shihpachungchi Formation, Eocene, (g) Tachien Sandstone, Eocene, (h) Colluvium, Pleistocene, and (i) Alluvium, Holocene. Each complex comprises different types of sedimentary rocks varying in strength. Interbedded sandstone, argillite, phyllite and slate dominate the rocks of Lushan Formation. Juifang Group, Cholan and Sanhsia Formations mainly comprise sandstone and shale. Hsitsun Formation includes the rocks of Slate, sandstone and phyllite. Shihpachungchi and Tachien Sandstone comprise sandstone, slate and shale. Alluvium and Colluvium contain weak sand, gravel and clay.

The CRW drains tropical monsoon climate zones. The mean annual rainfall is about 3267 mm and the mean annual temperature is 25.1°C. The relative atmospheric moisture averages 75.6%. In this region, the majority of rainfall occurs between June and October because periodic typhoons and trade wind can provide abundant moisture sources during wet season. Conversely, the Center Mountain usually blocks moisture brought by northwestern trade wind, leading to less rainfalls in other months during dry season.

Cishan River watershed drains the Western Foothills of Taiwan, which has a decadal erosion rate of ~30 mm/y. The Cishan River is a main tributary of the Kao-Pin River (the largest river of Taiwan for total river basin) that supplied 49 Mt./y during 1990 and 1999 and this value of

river-borne suspended-sediment discharge is only smaller than that supplied from the Beinan River (~88 Mt./y) in Taiwan [6]. The Water Resource Agency (WRA) of Taiwan continuously made stream gauging and a fortnight suspended-sediment sampling at the Shanlin Bridge station near the downstream from 1986 to 2005, restarting from 2010 till now. Based on the data recording at this gauging station, the Cishan River has a mean suspended-sediment concentration of about 696 ppm, annual sediment yield of about 1.06 Mt./y.

### 2.2. Catastrophic landslide in Hsiaolin Village

Hsiaolin village is a village on the foothill of Hsiendu Mountain in the Cishan River watershed. At 6:16 AM (local time) on 9 August in 2009, the catastrophic landslide was triggered on the hillslope of Hsiendu Mountain when rainfall reached 1676.5 mm equal to 72-hour accumulative rainfall obtained from the rainfall record of the Jiashan station, with the peak hourly rainfall intensity of 95 mm/h (**Figure 3**). This landslide is the largest landslide occurred during Typhoon Morakot, damming the near Cishan River channel and was break at about 7:40 AM on 9 August. This dam-break flood led to abrupt change in the water level of the Cishan River downstream area, and instrumental records on the downstream of the Hsiaolin Village indicated that 2.75 m drop during the period from 7:10 to 7:50 AM and 7.88 m rise during the period from 8:40 to 9:30 AM. Note that this evident water level changes in the Cishan River channel were observed at 27.8 km downstream of the Hsiaolin Village [44]. Total causality in Hsiaolin Village were more than 400 people dead and missing. The village itself no longer exists.

**Figure 4** shows the Formosat-II image and aerial photos of the Hsiaolin landslide. According to the digital terrain models (DTMs) with a resolution of 5 m established by the aerial photos

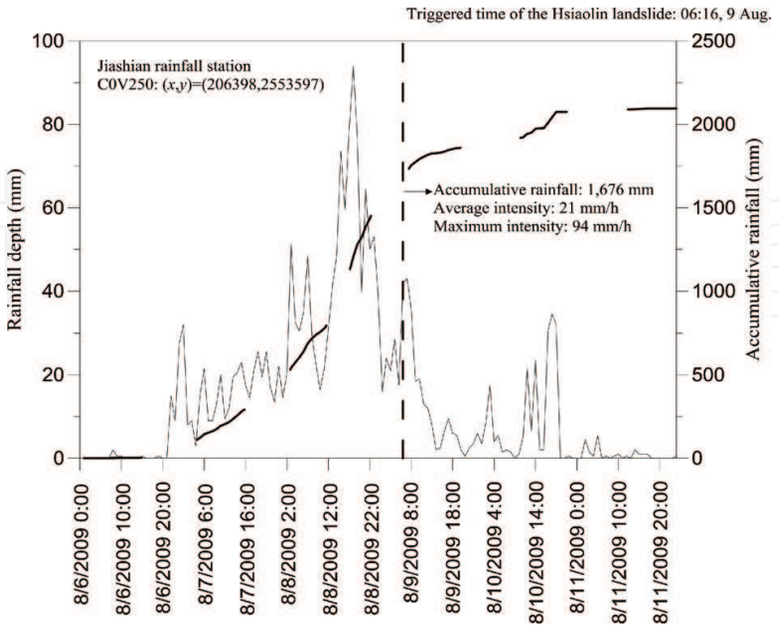


**Figure 3.** Hourly and accumulative rainfall for typhoon Morakot recorded by the Jiashan rainfall stations (11.4 km SSW of the Hsiaolin landslide) during the period from 6 Aug. to 11 Aug.

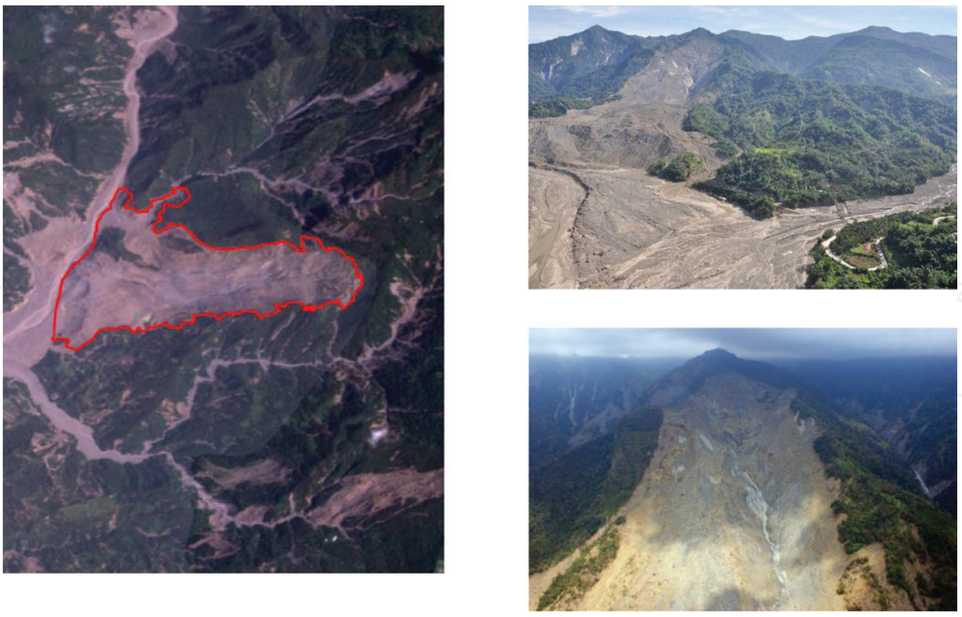

**Figure 4.** Formosat-II image and aerial photos of the Hsiaolin landslide in the Cishan River watershed, Taiwan.

provided by the Agricultural and Forestry Aerial Survey Institute of Taiwan, Kuo et al. [7] indicated that the major body of the Hsiaolin landslide had the extent of 57 × $10^4$ $m^2$ and was estimated to have a volume about 24 ± 2 million $m^3$, distributed at an average depth of 42 ± 3 m. Moreover, it is 3.2 km long in an E–W direction and 0.8 to 1.5 km wide. The total fall height was 830 m from the top of the head scarp, at an elevation of 1280 m, to the toe of the landslide deposit at 450 m [8]. Comparing the Hsiaolin landslide with the 1:25000 geologic map (provided by CGS, MOEA) shows that this landslide crops the late Miocene to early Pliocene Yenshuikeng Formation composed of mudstone, sandstone, and shale. Strength of sandstone is much greater than mudstone and shale, and its corresponding uniaxial compressive strength is about 15 Mpa [9]. The source area of the Hsiaolin landslide was the dip slope of the east limb of the syncline that could exhibits simple traces of strata on a horizontal cross-section, however, because the strata and slopes on the east region of the Cishan River shows the similar characteristics, the bedding traces have rather complicated patterns [8].

A cascade of loose sediment produced by the Hsiaolin landslide deposited on the Cishan River and generated the barrier lake that was suddenly broken about 1 to 2 hours after its generation. The landslide dam was estimated to have a volume of 15.4 million $m^3$. This is clear that only half of the total sliding mass contributed to the main body of the landslide dam [10]. The maximum elevation produced by this catastrophic landslide is about 475 m, on the west bank of the Cishan River and the maximum water level that can overtop the dam crest is about an elevation of 413 m. The height of the dam was about 44 m and the deepest deposit was a thick of 60 m. Moreover, this dam drained about 354 $km^2$ watershed area and trapped about 9.9 million $m^3$ water before overtopping occurred [10]. On the basis of data recorded by continuous river stream gauging from Shanlin Bridge station, the water level of the Cishan river dropped to 118 m nearly at 08:00 AM after the landslide dam formation and rapidly rise up to 126 m at about 9:40 AM [11]. Hence, we can infer that the landslide dam was suddenly flushed out by river water after the dam formation during the period of only 2 hours.

## 3. Methodology and results

### 3.1. Rainfall brought by typhoon Morakot

On August 8, 2009, Typhoon Morakot was "born" at approximately 22.4°N and 133.8°E in the North Pacific Ocean, about 1000 km far from Northeastern Philippines, moving west at a speed of 10–30 km/h towards Taiwan. In retrospect, Typhoon Morakot had not been considered a serious threat before striking Taiwan. However, contrary to the prediction, after landing Taiwan, it caused more damage than any other typhoon because of massive rainfall, especially in Taiwan's southwestern region. **Figure 5** shows the spatial distribution of rainfall in Taiwan for the six-day rainfall during Typhoon Morakot. This "monster "brought significant rainfalls causing severe debris flows, shallow and deep landslides, and debris dam-break in the mountainous areas of the central and southern Taiwan. Consequently, 675 people were dead; 34 people were hurt; the economic loss was up to 164 million NT dollars.

**Figure 6** shows the time series of hourly rainfall data and cumulative rainfall during Typhoon Morakot obtained from Alishan station in central Taiwan. On the basis of this hourly rainfall

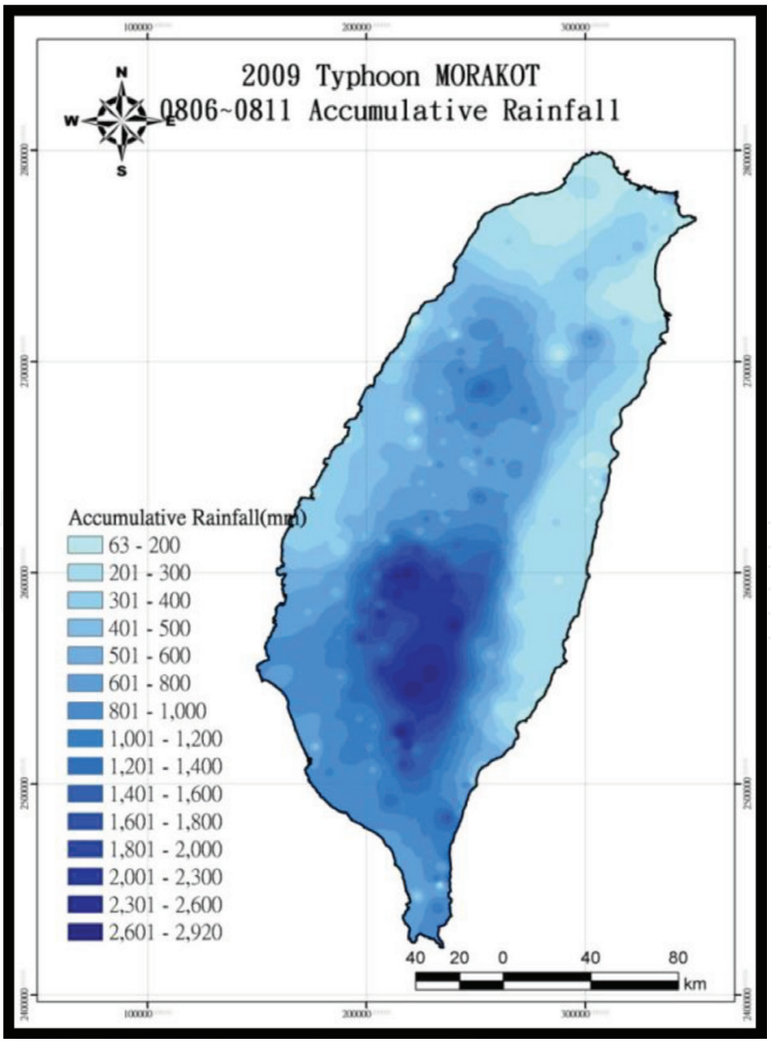


**Figure 5.** Spatial distribution of rainfall in Taiwan for Typhoon Morakot during six days.

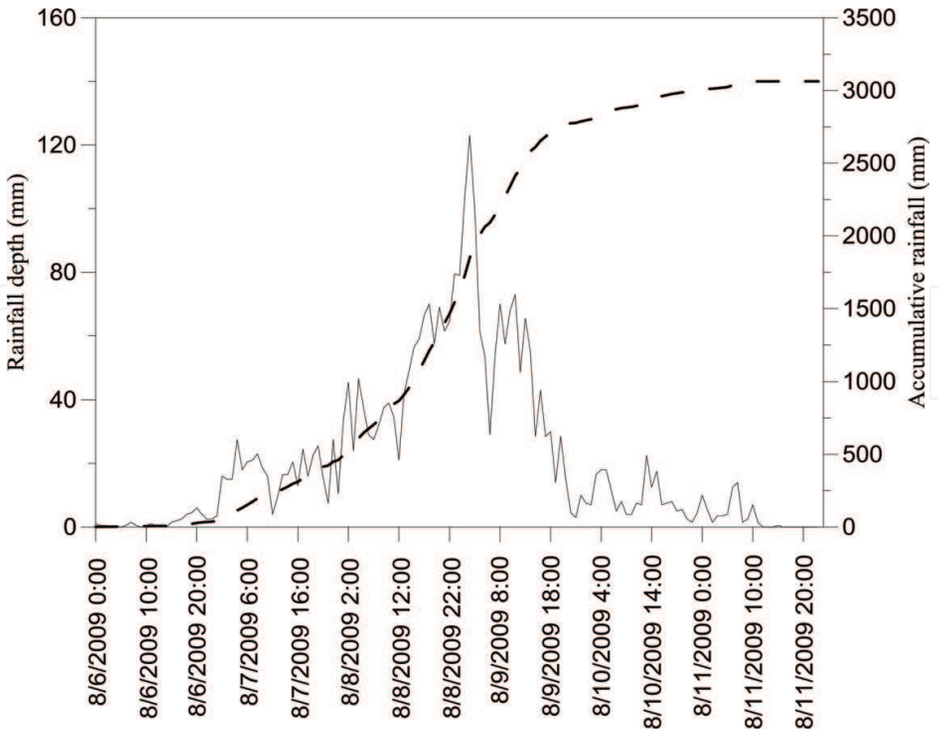


**Figure 6.** Time series of hourly rainfall amount and its accumulative rainfall from Aug. $6_{th}$ to the end of Aug. 8th in 2009. This rainfall data is obtained from the records of the Alishan station.

data, the maximum 1-hour, 6-hour, 24-hour, 48-hour and 72-hour rainfall near the headwaters of the Cishan River watershed were 123 mm, 549 mm, 1623 mm, 2361 mm and 2748 mm, respectively. Both the previous 1-hour (113 mm by Typhoon Herb) and 48-hour (1978 mm by Typhoon Herb) rainfall records were broken. The 24-hour and 48-hour rainfall records approximate the world record (1825 mm and 2476 mm, respectively) [12], as shown in **Figure 7**. Moreover, the return periods for 24-hour, 48-hour, and 72-hour rainfall at the Alishan station both exceeded

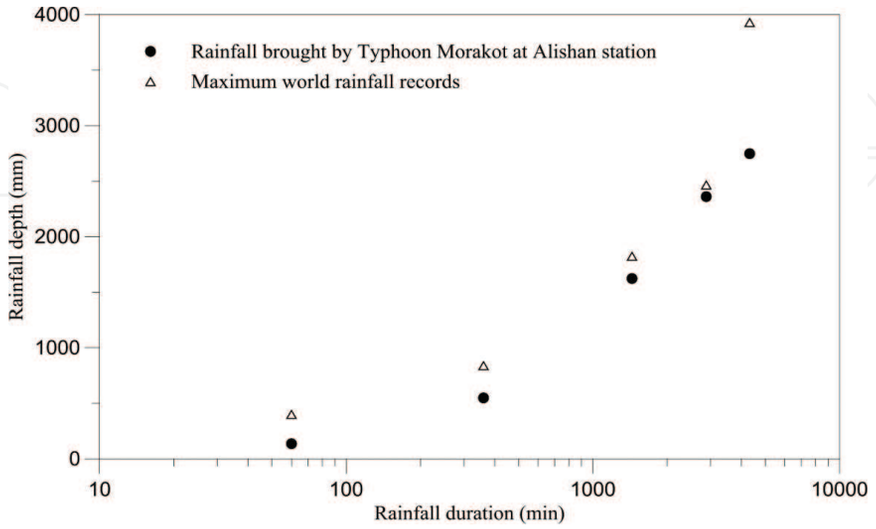


**Figure 7.** Diagram of rainfall depth-duration for Typhoon Morakot at the Alishan rainfall station near the Cishan River watershed in comparison with the maximum rainfall records in the world.

2000 years (WRA, 2010). Totally, Typhoon Morakot released about 3063 mm rainfall depth during 6 days. This total value is equivalent to about 90% of the annual rainfall in 2009 at Alishan station. In comparison with other typhoon storms, the magnitude of rainfall brought by Typhoon Morakot is quite huge as shown in **Figure 8**. These patterns indicate that this rainfall event can be characterized as high intensity, huge total accumulation and long duration in a large scale, and hence had generated severe hillslope erosion (e.g., landslides) in watersheds.

### 3.2. Landslides triggered in the Cishan River watershed

Taiwan has total landslides of 45,172 after the massive rainfall brought by Typhoon Morakot, ranging from 258 $m^2$ to 3,510,861 $m^2$ with an average of 12,488 $m^2$ (**Figure 9**). These landslides were identified and mapped from the fused Formosat-II images having resolutions of 2 m, with detailed field checking, and then were digitized into a geographic information system (GIS). Via the fused Formosat-II images (in 2008 and 2009), a pair of successive landslide inventories were mapped through the normalized difference vegetation index (NDVI). The NDVI data are helpful in determining the density of green planet presence via the wavelengths difference. Mathematically, the NDVI is expressed as follows [13]:

$$NDVI = \frac{NIR - IR}{NIR + IR} \tag{1}$$

where NIR is the near-infrared reflection and IR is the infrared reflection. These two reflections can be obtained by observing the different colors in wavelengths reflected by the plants. For landslide areas, the values of NDVI for a given pixel in the Formosat-II satellite images always range from −1 to 0.

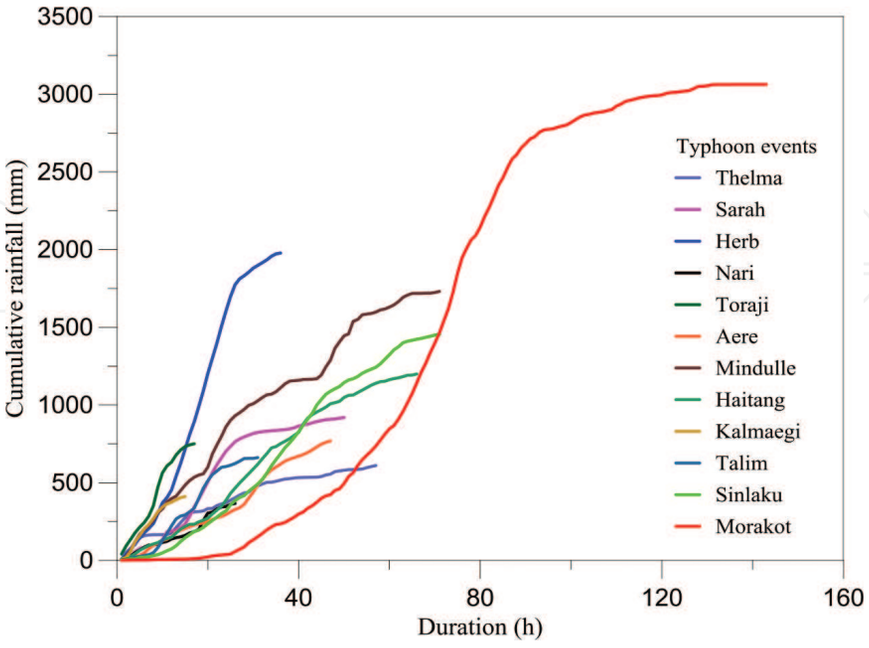


**Figure 8.** Cumulative rainfall in relation to its corresponding rainfall duration for different typhoons obtained from the records of Alishan rainfall stations.

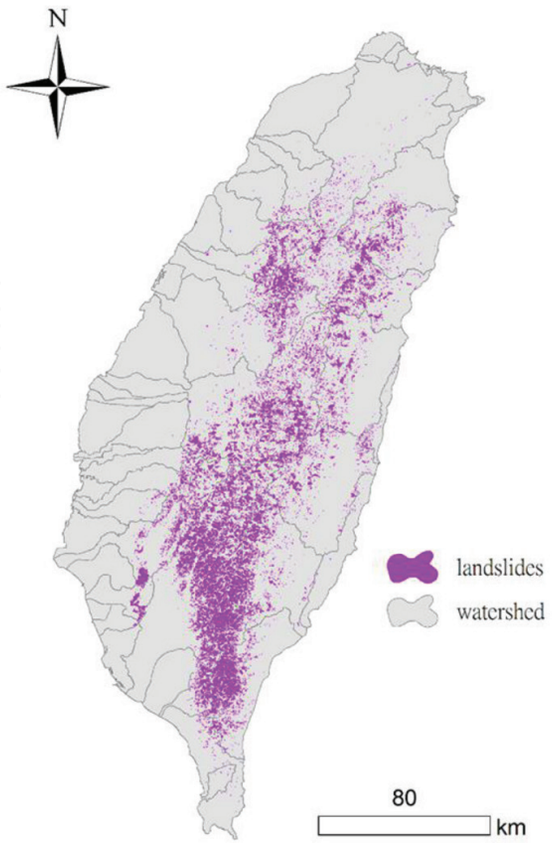


**Figure 9.** Location of landslides in Taiwan mapped after Typhoon Morakot. These 45,124 landslides range from 258 $m^2$ to 3,510,861 $m^2$, with an average of 12,488 $m^2$.

As shown in **Figure 9**, the landslide areas after Typhoon Morakot mainly concentrate on southern Taiwan that contains the Cishan River watershed (CRW). **Figure 10** shows the landslide area (see red colored regions in **Figure 8**) before (in 2008) and after (in 2009) Typhoon Morakot. In contrast, the total landslide area increased from 7.83 $km^2$ to 33.98 $km^2$ and the landslide density increased from $5.7 \times 10^{-3}$ no./ha to $28.4 \times 10^{-3}$ no./ha (total number of landslide/survey area) after the disturbance of Typhoon Morakot. On average, the mean landslide area is 0.012 $km^2$, ranging from a smallest area of 0.12 $m^2$ to a maximum value of ~2.49 $km^2$. These patterns indicate that Typhoon Morakot caused severe disturbances on the Cishan River watershed and could lead to significant changes in the geomorphic systems of this region, which we discuss later.

In addition, landslide rank against cumulative landslide area can exhibits the contribution of different landslide magnitude to erosion processes. In this investigation region, landslides were ranked in a series of numbers from the smallest area (No. 1) to the largest area (No. 2338), as shown in **Figure 11**. As a consequence, the largest 10 landslides (0.43% of total number) account for 27% of total landslide area, the largest 58 landslides (2.5% of total number) account for 50% of total landslide area, and the largest 649 landslides (27% of total number) account for 90% of total landslide area. This result indicated that large landslides can majorly dominate denudation processes in the CRW.

These landslide data were further analyzed by using a fractal model. The dependence of landslide frequency on landslide magnitude is an aspect of critical importance to hazard risk

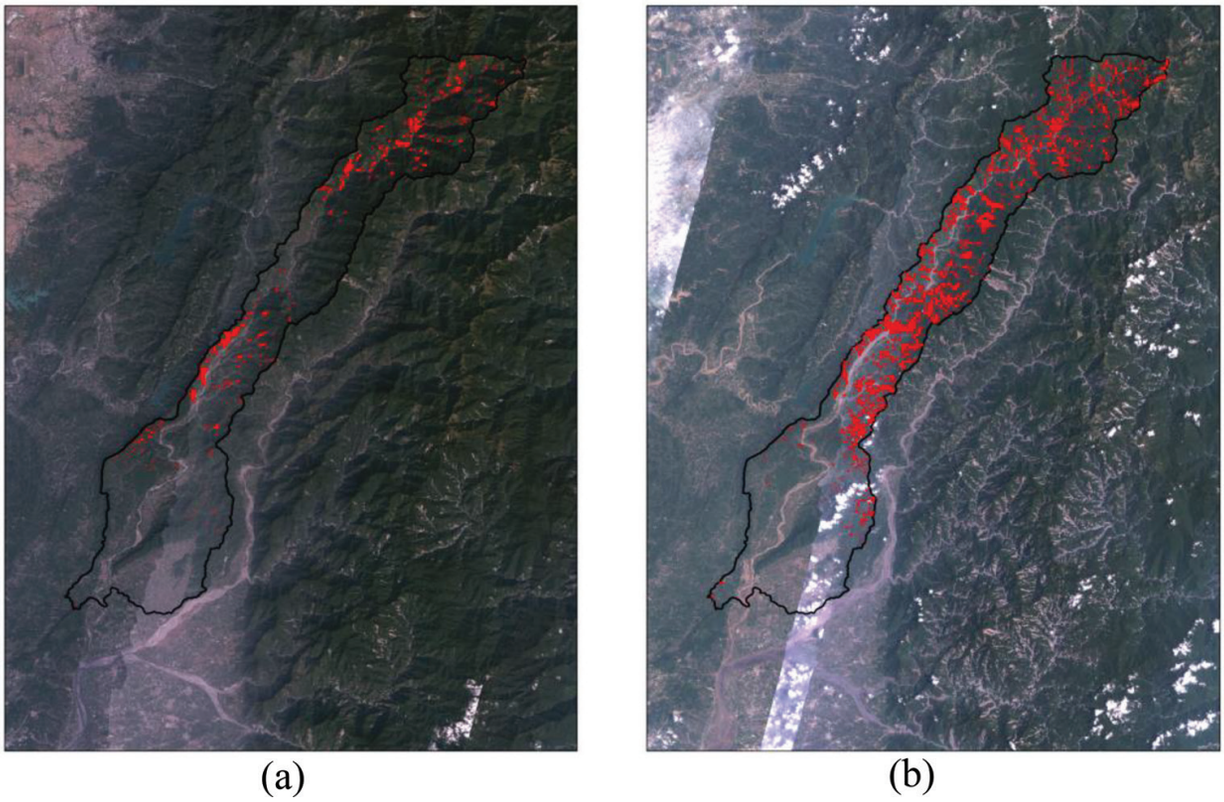


**Figure 10.** Landslide inventories mapped from a pair of Formosat-II satellite images in 2008 and 2009, respectively, for the Cishan River watershed. (a) Pretyphoon image in 2008. (b) Posttyphoon image in 2009.

assessment and management [14]. Based on the analysis of landslide inventories in worldwide regions, frequency distributions and PDFs (probability density functions) exist in landslide magnitude with heavy tail for medium and large landslides. The mathematical expression of this algebraic PDF right tail decay is generally explained as a linear fitting for power-law scaling [15–18, 45, 46]. Here we characterize the noncumulative frequency-area relations to clarify the landslide behavior in the CRW.

The present paper now considers the noncumulative relation as:

$$p(A_L) = CA_L^{-\beta} \tag{2}$$

where $A_L$ is the magnitude of landslide area, the $p(A_L)$ is a PDF (probability density function) equivalent to $\frac{1}{N_{LT}}\frac{\Delta N_L}{\Delta A_L}$, and the $\triangle N_L$ is the number of landslides with area between $A_L$ and $A_L + \triangle A_L$ and the $N_{LT}$ is the total number of landslides. The constants $C$ and $\beta$ are obtained from fitting medium and large landslides in order to detect the right heavy tailed decay of PDF through a power-law. We increase our bin width $\triangle A_L$ with increasing area $A_L$, so that bin widths are approximately equal in logarithmic coordinates. In the CRW, the noncumulative relation of the total 2338 landslides caused by Typhoon Morakot in 2009 based on Eq. 1 is given in **Figure 12**. Above the cutoff at 645 m$^2$, the landslides displayed power law frequency-area scaling with exponent, $\beta = 1.69$, intercept, $C = 60$, and a determination coefficient ($r^2$) of 0.99. This result was derived from the scaling of the landslide area between 645 m$^2$ and 2.48 km$^2$.

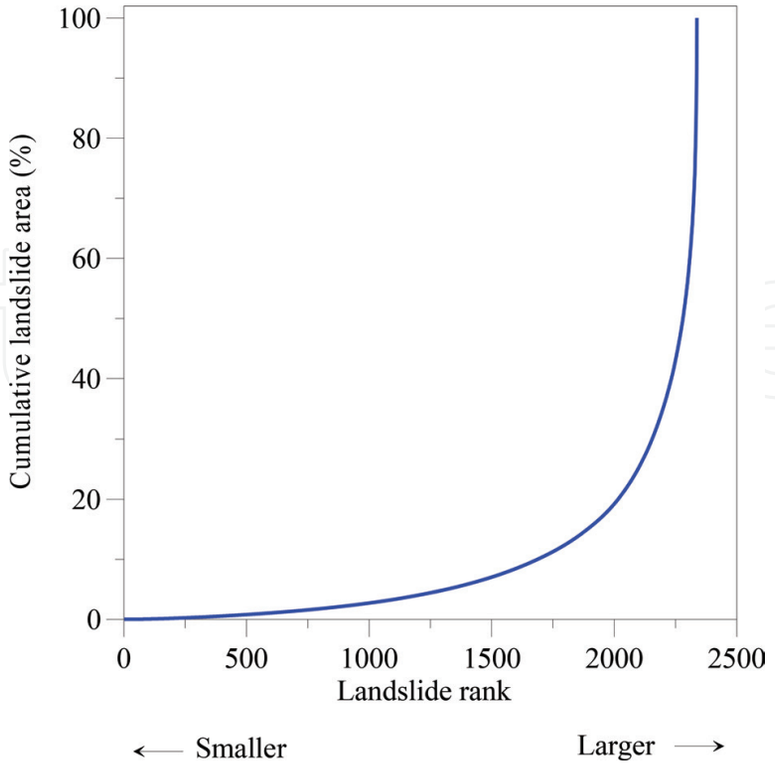


**Figure 11.** Cumulative percentage of landslide area against to the ranking numbers of 2338 landslides identified after typhoon Morakot in 2009 in the CRW. These landslides were ranked in a series of numbers from the minimum area (no. 1) to the maximum area (no. 2338). The cumulative area of the first 58 largest landslides accounts for 50% of the total landslide area while the first 649 largest landslides for 90% of the total landslide area.

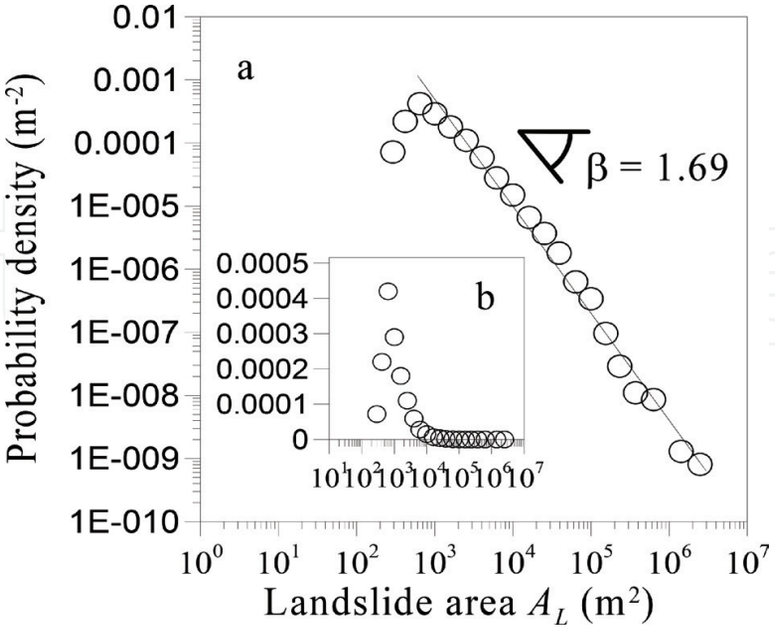


**Figure 12.** Noncumulative landslide frequency–area distributions in the CRW, based on landslide data after typhoon Morakot in 2009. The landslides of area larger than 645 m$^2$ display a fractal model with $\beta = 1.69$.

This phenomenon is described by self-organized criticality (SOC). Bak [19] indicates that if a system is well described by power-law scaling over a large portion of its event magnitude range, the system may be in a quasi-static state with SOC. In the CRW, landslides caused by Typhoon Morakot satisfies (2) with $\beta$ = 1.69 and suggest that landslide triggering has SOC in this region. **Table 1** lists the values of $\beta$ based on (2) for the frequency distribution of landslide area derived from the worldwide regions. In comparison, the value of $\beta$ in the CRW is smaller than 2.5 in this study, among the lowest observed worldwide [27], showing our study area has higher societal risk caused by the higher occurrence probability of large landslides.

### 3.3. Landslide triggering response to geomorphic characteristics on hillslopes

Landslides tend to occur in groups. Occurrence of landslides on hillslopes is therefore influenced by the geomorphic characteristics of subaerial surface because some geomorphic condition can provide suitable environments for the development of landslide. Hence, the investigation of landslide abundance and its corresponding spatial distribution in relation to the factors in situ is necessary for landslide hazard assessment. Here we used 5 × 5 m digital elevation model (DEM) (provided by Water Resources Agency, WRA) to analyze different geomorphic settings such as elevation, slope, aspect, surface residual, surface curvature, and fractal dimension in the CRW. Also, the distribution of lithologic complexes was obtained from the geological map provided by the Center of Geological Survey, Taiwan. These above mentioned factors were examined with the location of landslide triggering in the CRW, as tabulated in **Table 2**.

The percentage of landslide area ($C_a$) for a watershed is defined as the total landslide area ALT divided by the watershed area A, i.e., $C_a = A_{LT}/A$. Ca expresses the overall extent of damage caused by landslides done to the land [18, 28] and this proportional damage indicator is used

| Region | $\alpha$ | β |
|---|---|---|
| Japan [20] | 0.89 | 1.89 |
| Western Southern Alps, New Zealand (Hovius et al., 1997) | 1.1 | 2.1 |
| Challana Valley, Bolivia [21] | 1.6 | 2.6 |
| Alameda, USA [21] | 2.3 | 3.3 |
| Umbria, central Italy [22] | 1.5 | 2.5 |
| California, USA [22] | 1.3 | 2.3 |
| Lombardy, northern Italy [23] | 0.85 | 1.85 |
| Southern California, USA [24] | 1.1 | 2.1 |
| Fiordland, New Zealand [25] | 1.07 | 2.07 |
| Val di Fassa, Italy [26] | 1.56 | 2.56 |
| TWR and CYL watersheds, Taiwan [18] | 0.65 | 1.65 |
| CRW, Taiwan | 0.69 | 1.69 |

**Table 1.** Exponent values of fractal model for landslide frequency-area distribution collected form the worldwide observations.

| | Classification | $C_a$, % | $D_L$ | $R_L$, |
|---|---|---|---|---|
| Elevation | 0–500 | 0.52 | 2.89 | 1.17 |
| | 500~1000 | 1.47 | 8.19 | 11.74 |
| | >1000 | 2.67 | 14.89 | 6.92 |
| Aspect | North | 0.47 | 2.62 | 4.65 |
| | Northeast | 0.51 | 2.83 | 6.75 |
| | East | 0.62 | 3.43 | 6.64 |
| | Southeast | 0.70 | 3.91 | 5.95 |
| | South | 0.57 | 3.15 | 4.43 |
| | Southwest | 0.68 | 3.76 | 4.91 |
| | West | 0.63 | 3.50 | 4.26 |
| | Northwest | 0.49 | 2.76 | 3.56 |
| Slope gradient | S < =5% | 0.01 | 0.07 | 0.09 |
| | 5% < S < =15% | 0.08 | 0.42 | 1.06 |
| | 15% < S < =30% | 0.31 | 1.72 | 2.49 |
| | 30% < S < =40% | 0.46 | 2.55 | 4.29 |
| | 40% < S < =55% | 1.11 | 6.21 | 6.89 |
| | 55% < S < =100% | 2.45 | 13.67 | 8.05 |
| | S > 100% | 0.23 | 1.30 | 7.07 |
| Geologic settings | Loam | 0.08 | 0.45 | 0.76 |
| | Slate | 0.13 | 0.75 | 25.45 |
| | Interbedded slate and sandstone | 0.08 | 0.43 | 3.05 |
| | Interbedded sandstone and shale | 4.07 | 22.67 | 6.00 |
| | Hard sandstone | 0.13 | 0.73 | 4.46 |
| | Hard shale | 0.17 | 0.92 | 3.35 |
| | Gravel | 0.00 | 0.02 | 0.09 |
| Curvature | Convex | 1.98 | 11.03 | 4.40 |
| | Flat | 0.08 | 0.42 | 1.57 |
| | Concave | 2.60 | 14.50 | 5.71 |
| Surface roughness | 0~0.3 | 1.50 | 7.99 | 4.71 |
| | 0.3~0.6 | 2.03 | 10.81 | 5.19 |
| | 0.6~0.9 | 0.80 | 4.28 | 4.46 |
| | 0.9~1.2 | 0.23 | 1.25 | 4.45 |
| | 1.2~1.5 | 0.03 | 0.15 | 3.17 |
| | 1.5~1.8 | 0.00 | 0.02 | 6.54 |
| | 2~2.2 | 0.00 | 0.03 | 1.61 |

| | Classification | $C_a$, % | $D_L$ | $R_L$, |
|---|---|---|---|---|
| Fractal dimension | 2.2~2.4 | 2.47 | 12.96 | 6.43 |
| | 2.4~2.6 | 2.02 | 10.58 | 4.91 |
| | 2.6~2.8 | 0.08 | 0.42 | 0.66 |
| | 2.8~3 | 0.003 | 0.02 | 0.09 |

$C_a$ is the percentage of landslide area in the region in relation to total watershed area. $D_L$ is the landslide density equivalent to ratio of landslide number in the region to total watershed area. $R_L$ is the landslide rate equivalent to the percentage of landslide area in the region in relation to the corresponding region area.

**Table 2.** Landslide distribution in response to geomorphic and geologic settings in the CRW.

in the evaluation of other hazard [29]. Landslide density $D_L$ is the ratio of numbers of landslide to the watershed area. Landslide rate $R_L$ is the percentage of landslide area in the region of each geomorphic characteristic to the extent of geomorphic characteristics. These landslide variables can help us to clarify the landslide triggering in response to diverse geomorphic and geologic settings.

As shown in **Table 2**, landslide distributed in the different geomorphic and geologic settings cropping out CRW after Typhoon Morakot. The largest elevation group in the CRW is the region lower than 500 m that extends 44% of total watershed area. This region only cropped out $C_a$ of 0.52%, landslide density ($D_L$) of 2.89 No./km$^2$ and is covered 1.16% of total by landslides. The smallest unit is the region that its elevation is between 500 m and 1000 m, only accounting for 13.98% with landslide density of 8.19 of 2.89 No./km$^2$ and has landslide rate of 10.51%. In addition, the region of elevation higher than 1000 m has landslide density of 14.89 No./km$^2$ and landslide rate of 6.47%. Results show that landslides tend to occur at the region of elevation higher than 500 m on hillslopes.

On the basis of the Soil and Water Conservation Technical Guide issued from Taiwan government, the terrain gradient in the CRW can be categorized into seven classes as well as shown in **Table 2**. In this watershed, the hillslopes are most widely mantled by the sixth-class slope gradient (between 55% and 100%, i.e., between 28.8° and 45°; see **Table 1**), with 32.9% of the total watershed area (842 km$^2$) and has the greatest values for landslide density (13.67 No./km$^2$) and landslide rate (7.45%), respectively. In other words, the smallest unit is the gradient of hillslopes less than 5% (i.e., 2.86°) and therefore has the lowest values for landslide density of 0.07 No./km$^2$ and landslide rate of 0.09%. Aspects of hillslopes were also classified into eight groups (**Table 2**). It is clear that there are no evident differences in each hillslope aspect that accounts for about 8–15% of the total watershed area. The largest unit is west-facing slopes that extends 15.33% of the 843 km$^2$ CRW area, with the quite small values of landslide density (3.5 No./km$^2$) and landslide rate (4.68%). Of particularly, landslides in the CRW after Typhoon Morakot cropped out the similar values of $C_a$, $D_L$ and $R_L$ in eight aspect groups, ranging from 0.47 to 0.7%, from 2.62 No./km$^2$ to 3.91 No./km$^2$ and from 3.43 to 5.26%, respectively. These patterns suggest that there are no significant variations in landslide distribution in diverse hillslope aspects, indicating the aspect has low effect on landslide triggering.

The above mentioned geomorphic characteristics are usually used to be as landslide triggers, and to examine landside occurrence in response to geomorphic systems. However, those

geomorphic characteristics are simple and using those characteristics (i.e., elevation, slope and aspect) could not represent complex geomorphic systems in natural environments, e.g., convergent slopes and surface roughness. To consider the complexity of geomorphic conditions, we employed curvature, surface roughness and fractal dimension, comparing with the location of landslide occurrence to find out the 'hotspot' or 'prone area' in the CRW.

Curvature is the changing rate of slope along $x$ and y direction and can be categorized into three groups of divergent, flat and convergent based on curvature values of greater than zero, equal to zero and smaller than zero, respectively [47], as shown in **Table 2**. In comparison, divergent and convergent slopes individually lie the most regions of the total watershed area (about 47 and 48%). On the divergent slope, landslide triggering after Typhoon Morakot accounted for 1.98% of the total watershed area with 11.03 landslides per km$^2$ and landslide rate of 4.21%. In other words, the convergent slopes have 2.6% percentage of landslide area comparing with the area of the CRW, landslide density of 14.5 No./km$^2$ and landslide rate of 5.4%. Results show that both of divergent and convergent slopes can provide suitable condition for the development of landslides. Divergent slopes can lead to landslide triggering due to the effect of gravity along slope. Convergent slopes can concentrate water flow leading to increase in groundwater level and pore water pressure, therefore generating landslides on hillslopes. However, **Table 2** still indicates that landslides slightly tend to occur on convergent slopes in comparison with divergent slopes in the CRW. In addition, the flat region is not appropriate to landslide triggering and hence strictly has 0.42 landslides per km$^2$.

Here we define the surface roughness is a residual topography that can be derived from the cell by cell subtraction of original 5 × 5 m DEM and the mean of this DEM. Mean DEM was created by averaging elevation values within a 3-cell moving window. The raster of residual topography was then calculated as the cell-by-cell difference between the original DEM and the mean DEM. In the Cishan River watershed, surface roughness (i.e., residual topography) was calculated as the above mentioned flow and further categorized into six groups by 0–0.3, 0.3–0.6, 0.6–0.9, 0.9–1.2, 1.2–1.5 and 1.5–1.8. Based on this classification, the largest unit of surface roughness is the region of the values from 0.3 to 0.6 that covers about 39.32% of the total CRW area, with 10.81 landslides per km$^2$ respect to this region. Note that there is no significant difference between landslide rates in each surface roughness settings, ranging from 3.07% to 6.14%. These patterns suggest that landslides tend to be triggered in group in the region of surface roughness between 0 to 0.6. Above this cutoff, the landslide density and landslide rate evidently decrease as well as shown in **Table 2**.

In other words, natural landscapes generally have fractal characteristics. Terrain can be considered self-similar in the two horizontal directions and self-affine in cross-section [30]. This leads to the discussion of the relationships of landslide triggering with respect to the self-similarity or fractals of topography be necessary. Fractal dimension in the CRW was calculated using the Landserf software on the basis of 5 × 5 m DEM, comparing with the location of landslide occurrence. Landserf implements the variogram method (e.g., [31]), which we use in this study. The variogram is calculated as:

$$D = \frac{1}{2n(h)} \sum_{i=1}^{n} \sum_{j=1}^{n} \left(z_i - z_j\right)^2 \tag{3}$$

where *h* is the lag between measured cells and n is the number of pairs considered. Landserf calculates *D* within a moving window around each cell across the raster. This calculation can represent how the surface roughness/complexity changes over the study area. *D* is computed at different window sizes for n ≥ 9 and its value is between 2 (flat surface) and 3 (a space filling rough surface). In the CRW, the fractal dimension of land surface was digitalized in Landserf, then comparing with the landslide inventory after Typhoon Morakot (**Table 2**). Classification of fractal dimension in the CRW is defined as 2.0–2.2, 2.2–2.4, 2.4–2.6, 2.6–2.8 and 2.8–3. Results show that the most regions have the values of fractal dimension from 2.2 to 2.4 and from 2.4 to 2.6, accounting for 38.45% and 40.54%, respectively. Meanwhile, percentage of landslide area, landslide densities and landslide rates are quite larger in these regions (*D* values between 2.2 and 2.4 and between 2.4 and 2.6) than that in other regions. In particular, total landslide density is very high with 23 No./km$^2$ in the regions of *D* values ranging from 2.2 to 2.6, indicating that landslides tend to occur in this region.

In general, Geologic settings determine the strength of rocks that can further influence sediment production caused by weathering processes on hillslopes. Soft rock can usually lead to weak resistance to erosion. Based on geologic map provided by Central Geological Survey, MOEA, Taiwan, we can find that the largest geologic unit is interbedded sandstone and shale, cropping out about 72% of the total CRW area. We also examined landslide distribution in response to geologic settings. Results show that percentage of landslide area $C_a$, landslide density $D_L$, and landslide rate $R_L$ are 4.07%, 22.67 No./km$^2$ and 5.66%, respectively, in the region of interbedded sandstone and shale and these values are much greater than that in other regions, as shown in **Table 2**. Other regions crop out geologic units of gravel, loamy sand, slate, interbedded slate and sandstone, hard sandstone, and hard shale, respectively. These geologic units are usually recognized as hard rocks and structural settings. Although some of them are composed of loose materials that are tended to landslide triggering (loamy sand and gravel), but just crops out only 10.83 and 4.52% of total watershed area in the CRW.

The geologic setting crops out interbedded sandstone and shale that has weak, low resistance to erosion and lies most regions of the CRW, favoring the generation of landslides on hillslopes.

The above landslide inventory shows that landslide triggering can be influenced by geomorphic and geologic settings. The hillslope with elevation of 500 m, slope between 28.8° and 45°, convex slopes, surface roughness index from 0 m to 0.6 m, fractal dimension from 2.2 to 2.6 and geologic unit composed of sandstone has high potential for the development of landslides.

### 3.4. Aftermath of typhoon Morakot in the CRW

Denudation processes play a very important role in the fluvial systems of a watershed. A large amount of sediment materials produced by landslides could be entrained downslope from hillslopes into river channels, influencing the evolution of river morphology. Typhoon Morakot led to severe hillslope erosion in the CRW (**Figure 8**), and its consequent generation of sediment materials could deposit on hillslopes and river channels, changing the geomorphic response of the CRW. Here we compared the river borne suspended sediment and river bathymetry of the Cishan River to show the aftermath effect of Typhoon Morakot on the CRW.

*3.4.1. Changes in river-borne suspended sediment concentrations*

River-borne suspended sediment is an important feature of the global denudation system and is often adopted as a measure of terrestrial erosion rates and the intensity of erosion processes in watersheds [32, 33]. Here we quantitative the impact of Typhoon Morakot on the sediment loads of Cishan River by using the measurement of suspended-sediment discharge of Shenlin-bridge river stage station from 1987 to 2005 and 2010 (no measurement from 2007~2009). The water discharge is daily recorded, and the sediment concentration is measured fortnightly using a USDH-48 suspended-sediment sampler from the Water Resources Agency of Taiwan. Evaluating the amount of sediment loads can use the formula of rating curve based on water discharges. Fitting the plots of suspended-sediment discharge on log-log scale using least square can obtain an equation as

$$C_s = aQ^b \tag{4}$$

where $C_s$ is sediment concentration (ppm), $a$ is the unit sediment concentration and $b$ is the sediment mobilization capacity of water discharges. By fitting model curves based on (5) to both pretyphoon (from 1987 to 2005) and posttyphoon (in 2010) data, while keeping the exponent fixed to permit comparison between models, we obtained model coefficients $a_{pre}$ and $a_{post}$. The ratio of $a_{post}$ to $a_{pre}$ denoted by $\triangle a$ that can be used to estimate the influence of Typhoon Morakot on the fluvial system of the CRW. If $\triangle a > 1$, it means unit sediment concentration increased after the typhoon events.

**Figure 13** shows the river-borne suspended-sediment rating curves of the Cishan River on the basis of data recorded by the Shanlin Bridge gauge. The power-law relation of measurement data before Typhoon Morakot (from 1987 to 2005; see red line) fitted by least-square regression is expressed as

$$C_s = 16\,Q^{0.7} \tag{5}$$

and the relation of that after the typhoon events (in 2010; see black line) fitted by least-square regression is expressed as

$$C_s = 160\,Q^{0.7} \tag{6}$$

According to (5) and (6), change in unit sediment concentration for the Cishan River after Typhoon Morakot is equivalent to 10 (i.e., $\triangle a = 10$). Suspended-sediment concentrations in the Cishan River after the disturbance of Typhoon Morakot are as much as 10 times greater than decadal background value. This elevated posttyphoon erosion rate has resulted from the abundant landslide triggered by the typhoon events, and led to rich sediment supply from the hillslopes into river channels.

Here we calculated the annual river-borne suspended-sediment loads via the estimates of the rating curve for the Cishan River that combines the relationship of suspended-sediment concentration with respect water discharges, with the instrumental records of daily water discharges. In addition, we estimated the suspended-sediment loads driven by Typhoon

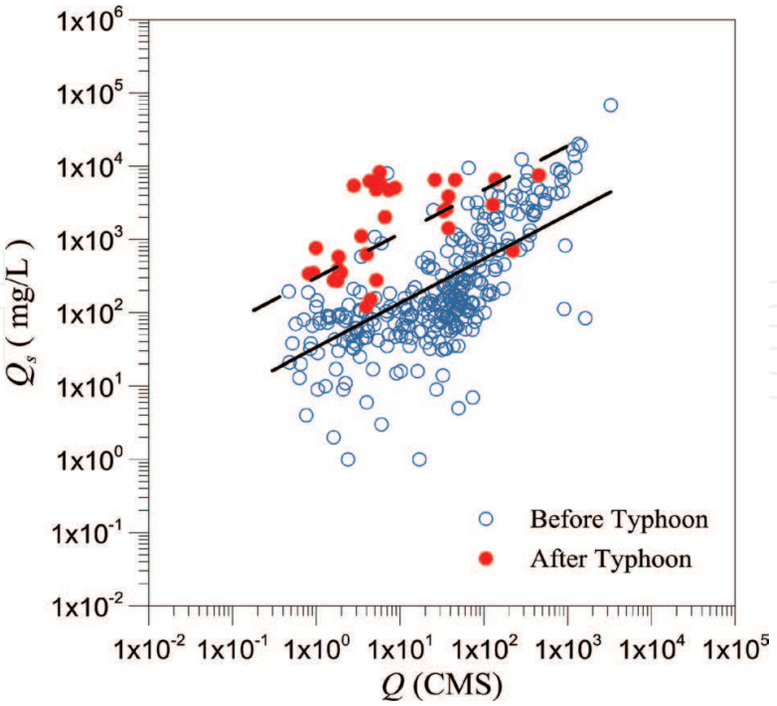


**Figure 13.** Suspended-sediment rating curves for the Cishan River. Red circles show measurements made before Typhoon Morakot; blue circles show measurements after the typhoon storms. Dashed lines are power-law relations fitted to pretyphoon data using log-transformed least-squares regression; solid lines are power-law relations fitted only to posttyphoon data.

Morakot for the Cishan River by the rating curve regression employing 4 successive daily water discharges at the beginning of 6 Aug. Note that all the records of daily water discharges were obtained from the Shanlin Bridge gauge.

**Figure 14** shows the mean annual sediment load, $Q_{sy}$, the annual sediment load in 2009, $Q_{s09}$ and the sediment load brought by Typhoon Morakot, $Q_{sm}$ for the Cishan River. On average, the annual river-borne suspended-sediment loads were ~ 1.06 Mt./y for the Cishan River. The total mass flushed out from the Cishan River watershed in 2009 was about 0.71 Mt. and, 0.64 Mt. of which was mobilized by Typhoon Morakot. It shows that Typhoon Morakot determined erosion processes on hillslopes, removing the most sediment materials from the CRW and accounted for 91% of total river-borne suspended-sediment during the period of 4 days. Only about 10% of sediment materials (~0.06 Mt) was transported by the Cishan River during the other period in 2009. Moreover, four-day suspended-sediment loads generated by Typhoon Morakot reached 61% of the decadal mean annual value.

*3.4.2. Changes in the riverbed elevation of the Cishan River*

In general, in mountain belts, sediment produced by storm-triggered landslides usually rapidly transfers into the fluvial systems and could not taking a long time to storage on hillslopes. However, we have shown a large amount of sediment materials deposited on hillslopes at the end of 2010 after Typhoon Morakot in the above section. Landslides caused by Typhoon Morakot supplied magnificent sediment to the Cishan River and could lead to sedimentation in the river channels. Here we collected the elevation data for the 62 cross section of

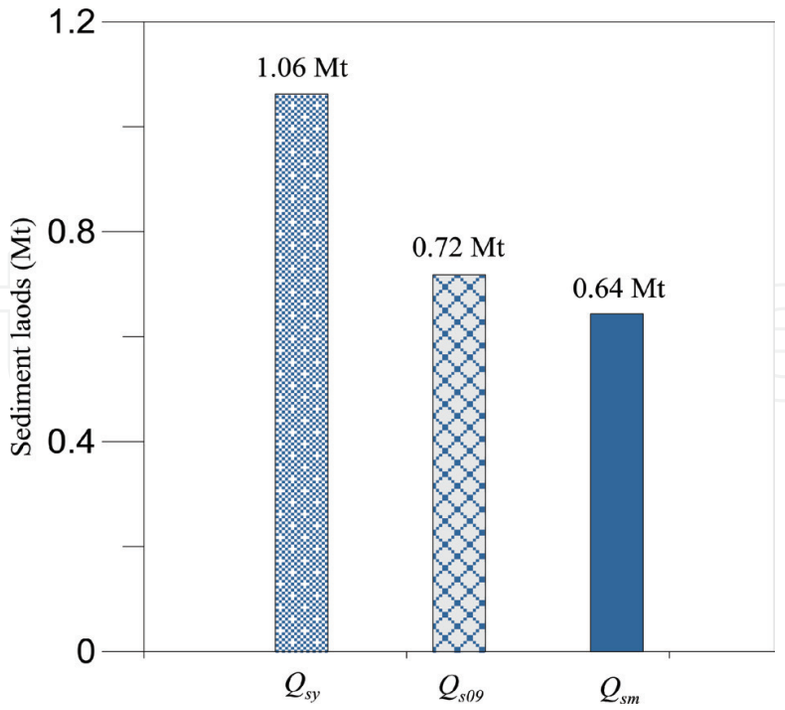


**Figure 14.** Mean annual sediment loads, $Q_{sy}$, annual sediment loads in 2009, $Q_{s09}$ and sediment loads brought by Typhoon Morakot, $Q_{sm}$ in the Cishan River derived from rating curve estimates.

the Cishan River, from Jiashian weir to Erren-Yuemei weir and the river reach is shown in **Figure 15**, which was reported by Water Resources Planning Institute [34].

The longitudinal profile is a continuous line by the lowest elevations at each stream cross sections. **Figure 16** shows the longitudinal profile of this 22.8 km river reach for the Cishan River, illustrated by the measurement data of each stream cross section during the periods of pretyphoon (in 2005) and posttyphoon (in 2010). Result indicates that the riverbed has a slight scour cumulative distance of below 1 km and above 18 km for the original cross section No. 22, respectively, but other reaches had significant sedimentation. To quantitative the effect of changes in the riverbed on the transport capacity for this river reach (**Figure 15**), the unit stream power [35] was used as

$$\omega = \rho g Q S / w \tag{7}$$

where $\omega$ is the unit stream power on river bed (W/m$^2$), $\rho$ is water density (1000 kg/m3), $Q$ is discharge of river channel (m$^3$/s), $S$ is the gradient of river channel and $w$ is channel width (m). In Taiwan, the channel width can be represented as [6]

$$w = Q^{0.5} \tag{8}$$

replacing the $w$ (7) by Eq. (8), we can obtain as following equation:

$$\omega = \rho\, Q^{0.5}\, S \tag{9}$$

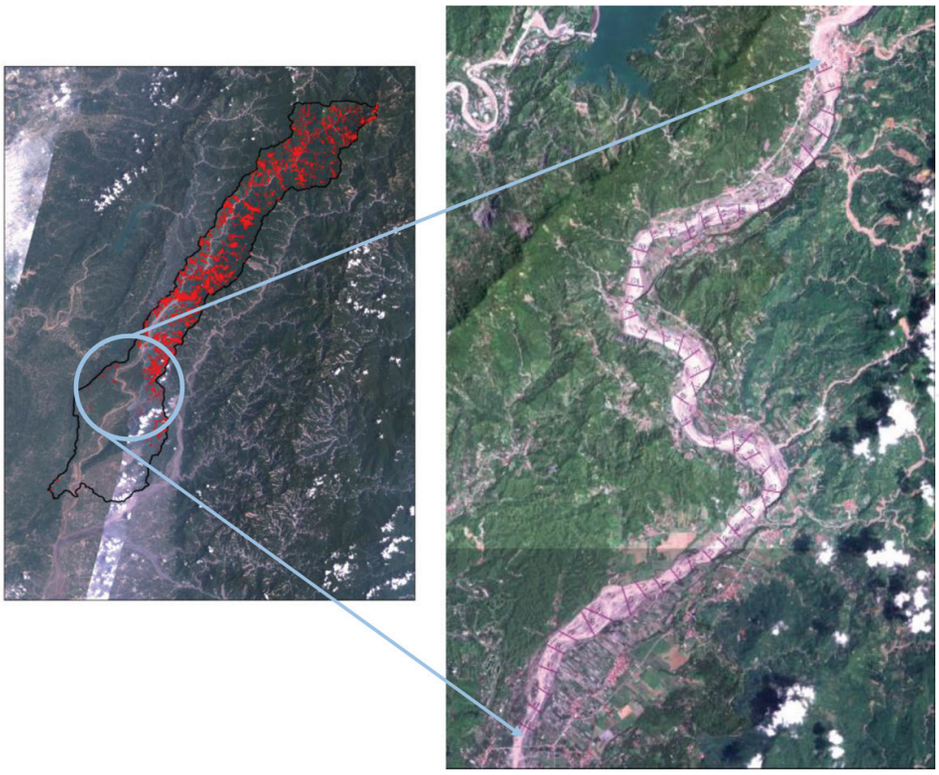

**Figure 15.** Formosat-II images of river reach with 62 cross section measurement for the Cishan River from Jiashiang weir to Erren-Yuemei weir.

Of particular interest, (9) infers that unit stream power could be only influenced by changes in the gradient of riverbed, because water density and water discharges could be treated as the same values in the same stream reach. Hence, based on (9), we can only examine the gradient of riverbed pretyphoon and posttyphoon to describe shifts in unit stream power for the river reach as shown in **Figure 16**. Calculating the gradient of longitudinal profile for the river reach form the measurement data in situ show that the pretyphoon riverbed gradient (in 2005) was 2.8% and the posttyphoon riverbed gradient (in 2010) was 1.3%, respectively. This indicates that unit stream power for the Cishan River had been significantly decreased (about 55%) after the disturbance of Typhoon Morakot and could lead to the lowering of transport capacity for the fluvial system, increasing sedimentation on the riverbed.

In other words, the longitudinal profile for the river reach is further separated into four parts with the cumulative distances of ~5 km, dissecting shifts in the unit stream power the river channels influenced by Typhoon Morakot. **Figure 17** shows the variations in the gradients of the riverbed calculated by the pretyphoon and posttyphoon measurement data in situ. Before the typhoon disturbance in 2005, the gradients of the riverbed were 0.00794, 0.00539, 0.00586 and 0.00705 for the upstream to the downstream, indicating that unit stream power in the river reach gradually decreased along the longitudinal river profile and had an increase in the riverbed gradient approximating the Erren-Yuemei weir. Sedimentation in the river

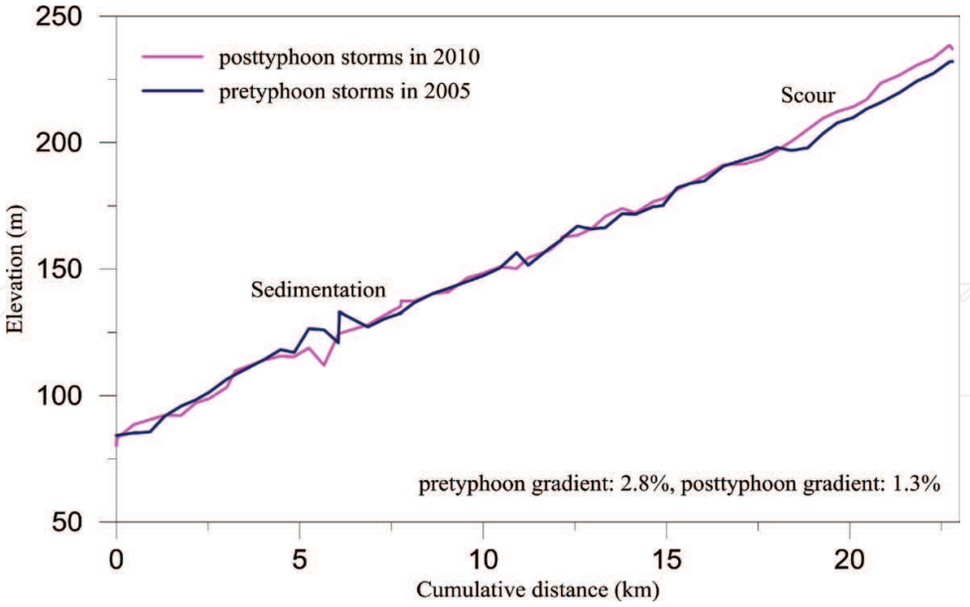


**Figure 16.** Longitudinal profiles of river reach for the Cishan River from Jiasiang weir to Erren-Yuemei weir obtained from the elevation data of pretyphoon and posttyphoon measurement.

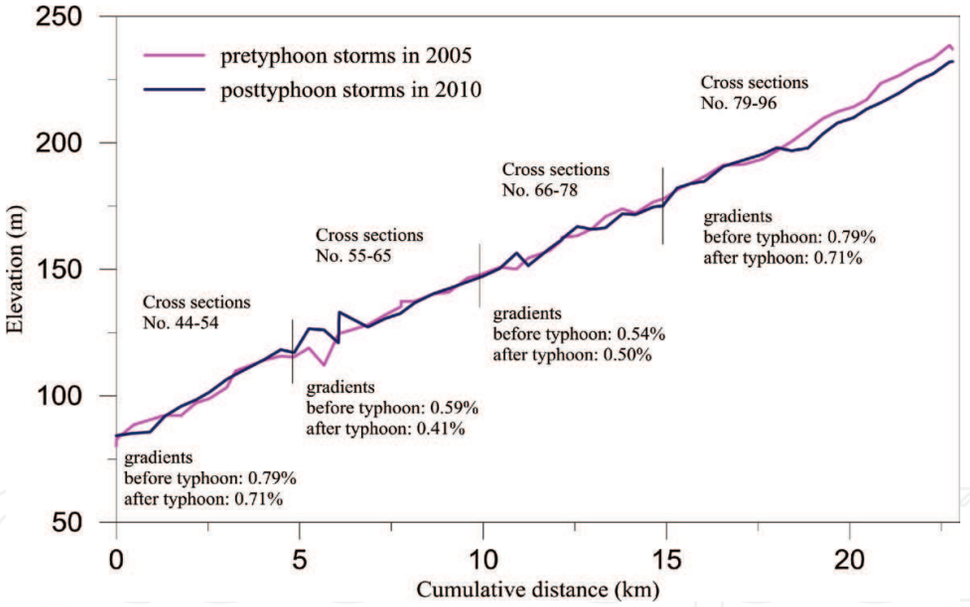


**Figure 17.** River gradients of four reaches along the Cishan River from Jiasiang weir to Erren-Yuemei weir before and after the disturbance of Typhoon Morakot.

channel was elevated by TypvMorakot, leading to reduction in its riverbed gradient and lowered about 10, 7, 29 and 7% of unit stream power for those four river reaches from the upstream to the downstream. These patterns suggest that significant sedimentation processes can be observed in this reach for the Cishan River, because the lowering of river transport capacity and abundant sediment supplied from the hillslopes in the CRW after Typhoon Morakot. Hence, the increased likelihood of flood inundation in the reach of the Cishan River (**Figure 14**) are expected due to its elevated riverbed.

### *3.4.3. Widening of the Cishan River*

Sediment sources produced by Typhoon Morakot was richly supplied from hillslopes to the fluvial system, elevating the riverbed of the Cishan River. This elevated riverbed lowered the unit stream power of the river channel and could lead to water flow centrally erode the riverbanks. To investigate changes in the riverbanks for the Cishan River, we used a pair of Formosat-II images to digitalize the pretyphoon (in 2008) and posttyphoon (in 2009) edges of the riverbanks within GIS. Then, HEC-RAS was used to extract the river widths per 100 m along the river channel before and after the disturbance of Typhoon Morakot. **Figure 18** shows the box-whisker plot of the river widths estimated from pretyphoon and posttyphoon data for the Cishan River. The second and third quartiles of the pretyphoon river widths are ~110 and 190 m, respectively, with a maximum of 728 m, a minimum of 16 m, and an average of 144 m. However, after the typhoon disturbance, the Cishan River widths were evidently widened and had the second and third quartiles of 260 and 471 m. Its maximum and minimum river widths were shifted into 2090 and 17 m, with an average of 342 m. This is clear that river widths increased by more than a factor of 2 to those statistical estimate values before the hit of the typhoon. Results show that Typhoon Morakot caused severe riverbank erosion for the Cishan River, leading to its consequent river width widening.

Comparing these two river channel inventories (in 2008 and in 2009) can show changes in river widths caused by Typhoon Morakot. Subtraction between the pretyphoon and posttyphoon river widths in each river cross section indicates that only about 22 cross sections display contracting adjustment, i.e., the river widths in 2009 smaller than that in 2008, only accounting for

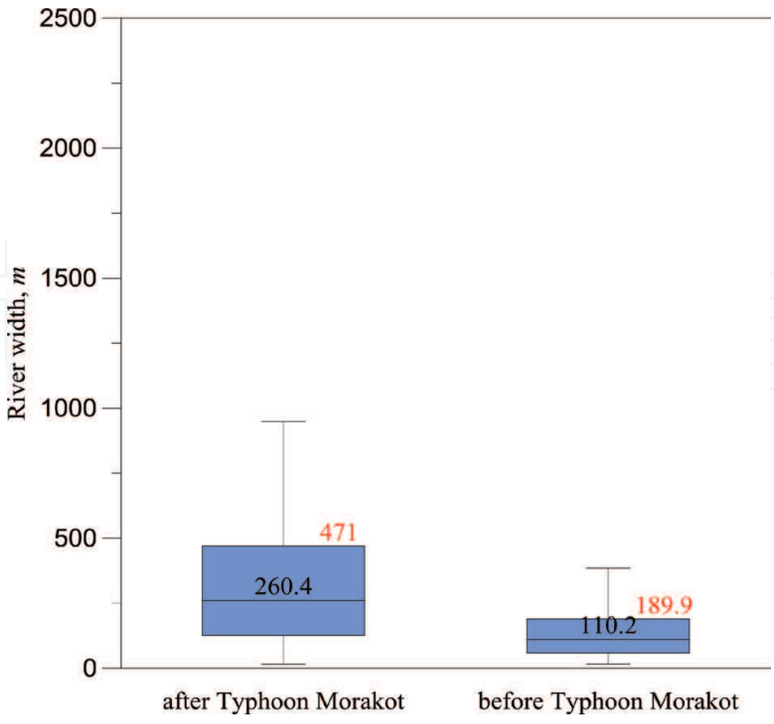


**Figure 18.** Box and whisker plot of river widths along the Cishan River estimated from pretyphoon and posttyphoon mapping based on a pair of Formosat-II images in 2008 and 2009, respectively.

1.6% of total 1357 cross sections. Most of the river widths show widening adjustment after the typhoon disturbance. Here we focused on the widening adjustment of the 1335 cross sections for the Cishan River in 2009. Also, we characterized the noncumulative frequency-widening relations to clarify whether the river widening has a SOC phenomenon. The noncumulative frequency distribution of river widening can be mathematically expressed as

$$p(R_w) = \alpha R_w^{-\beta} \tag{10}$$

where $R_w$ is the magnitude of river widening, the $p(R_w)$ is a PDF (probability density function) equivalent to $\frac{1}{N_w}\frac{\Delta N_w}{\Delta R_w}$, and the $\triangle N_w$ is the number of cross sections with widening between $R_w$ and $R_w + \triangle R_w$ and the $R_{wT}$ is the total number of river cross section widening. The constants $\alpha$ and $\beta$ are obtained from fitting medium and large river widening in order to detect the right heavy tailed decay of PDF through a power-law. We increase our bin width $\triangle R_w$ with increasing area $R_w$, so that bin widths are approximately equal in logarithmic coordinates. **Figure 19** shows that river widening having $R_w$ larger than 64 m could be well interpreted by a power-law statistic with $\alpha = 25.6$ and $\beta = 1.93$ with $r^2 = 0.98$.

Of particular interest, the $\beta$ value for river widening is greater than that for landslides driven by the same external trigger, i.e., Typhoon Morakot, suggesting that the occurrence likelihood of large magnitude of river widening is smaller than that of large landslides in the CRW for the perspective of environmental risks. Also, typhoon-induced river widening could have self-organized criticality. However, the $\beta$ values in (10) are very limited on the basis of worldwide observations and are not like the $\beta$ values in (2) for landslides that can be obtained

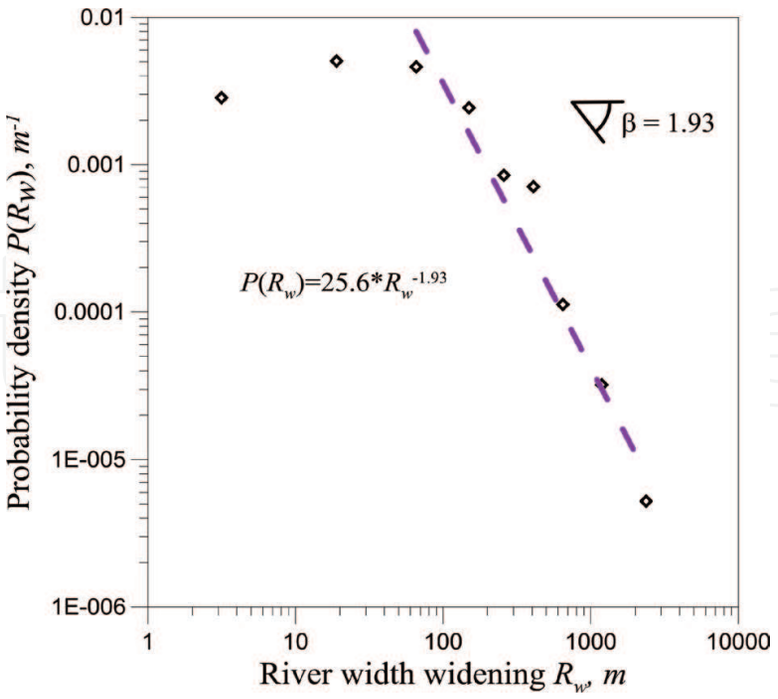


**Figure 19.** Noncumulative frequency distribution of river width widening after Typhoon Morakot for the Cishan River. Above the cutoff of 64 m, the river width widening satisfies a power-law relation with exponent β = 1.93.

from the many regions of the globe. Hence, more data of river channel inventories and its corresponding field checking should be necessary to examine whether the $\beta$ values in (10) still holds on true in other environments, or these values have a variation.

## 4. Discussion

In this chapter, we characterize landslides triggered by Typhoon Morakot in 2009, and its corresponding frequency-area distribution. Results show that the exponent value of a noncumulative relation for these landslides approximates the lowest limitation of worldwide observation. This infers that the hillslopes of the CRW has high potentials on landslide triggering. Meanwhile, ambient sediment materials produced by landslides could deposit on hillslopes and river channels and cause the adjustments of hillslope and fluvial systems, which can be observed from raised river-borne suspended-sediment concentration in the Cishan River (i.e., rich-supply hillslopes) and its decreased stream power (severe sedimentation in river channels). These patterns indicate that landslides not only pose threats to people's life and properties, but also have significant influence on the downstream. Hence, long-term and short-term strategies for landslide countermeasures are both necessary. The long-term strategies are the comprehensive management and regulation of basins and watersheds. The short-term strategies are the development of real-time warning systems for landslide triggering on hillslopes. In Taiwan, the present real-time warning system developed for landslide hazards are described as follow.

### 4.1. Landslide warning system adopted by the Taiwan's government

Before hit by this typhoon storms, the Central Geological survey, MOEA (2009) in Taiwan has used logistic equation to estimate landslide ratios via the potential values obtained from the combination of 100-year return period hourly rainfall depth and cumulative daily rainfall to map the landslide susceptibility. On the basis of this susceptibility, Taiwan's hillslopes were categorized in three regions of high risk, medium risk and low risk. Comparing with the location and initiation time in situ of landslides or rock avalanching (total of 909; provided by Soil and Water Conservation Bureau and Central Geologic Survey) show that these geomorphic erosion processes crop out the regions of high risk ~43% of totals. 90% of total can be observed when we consider both of high risk and medium risk regions. However, although the construction of landslide susceptibility can provide some useful information on mapping landslide-prone areas, the effect of real-time rainfall during typhoon storms should be necessary for landslide warning, still. Considering only landslide-prone area could also lead to the over-issued orders of hazard mitigation from landslide warning and also the wasting of governmental administrative resources.

Rainfall brought by typhoon storms plays a majorly important role in triggering landslides on hillslopes. Typically, some topographic and geologic regimes could provide suitable conditions for landslide triggering but landslides are still needed to be initiated by external triggers such as rain infiltration and its consequent saturation. The evolution of soil pore pressure can

be mainly influenced by these triggers, leading to the change of normal and shear stresses for a soil profile, further reducing slope failure [36, 37]. Many researchers have investigated landslide and debris flow triggering in response to different rainfall parameters [18, 38–40, 42, 43], showing that different rainfall characteristics can affect the initiation of debris flows and landslides from place to place. The precise relationship between landslides and rainfall parameters remains unclear, leading to the need of studies on the characteristics of rainfall-triggered landslides on hillsides in different regions [18].

To analyze the relationships of landslide triggering with respect to rainfall characteristics, Jan [41] collected 15 landslide inventories for different periods, comparing with its corresponding different rainfall parameters that include 3-hour average rainfall intensity $I_3$, 6-hour average rainfall intensity $I_6$, 12-hour average rainfall intensity $I_{12}$ and 24-hour average rainfall intensity $I_{24}$, obtained from the records of near rainfall stations. Results indicate that the strongest correlation is between landslide occurrence and 3-hour average rainfall intensity based on logistic regression analysis, with determined coefficient $r^2$ equivalent to 0.679. In other words, **Figure 20** shows the relationships between different average rainfall intensities (i.e., $I_3$, $I_6$, $I_{12}$ and $I_{24}$) and accumulative rainfall amount calculated from hourly rainfall data recorded by the Shinfa gauge. Red dots represent landslides occurred in that rainfall event and triangles represent no landslides occurred in that rainfall event (see **Figure 20**). These patterns suggest that $I_3$ can be recognized as a suitable indicator to the warning of rainfall-induced, shallow landslide [41].

In Taiwan, the rainfall-threshold warning system is well constructed for debris flow mitigation. Referring the rainfall parameter considered in the warning system for debris flow

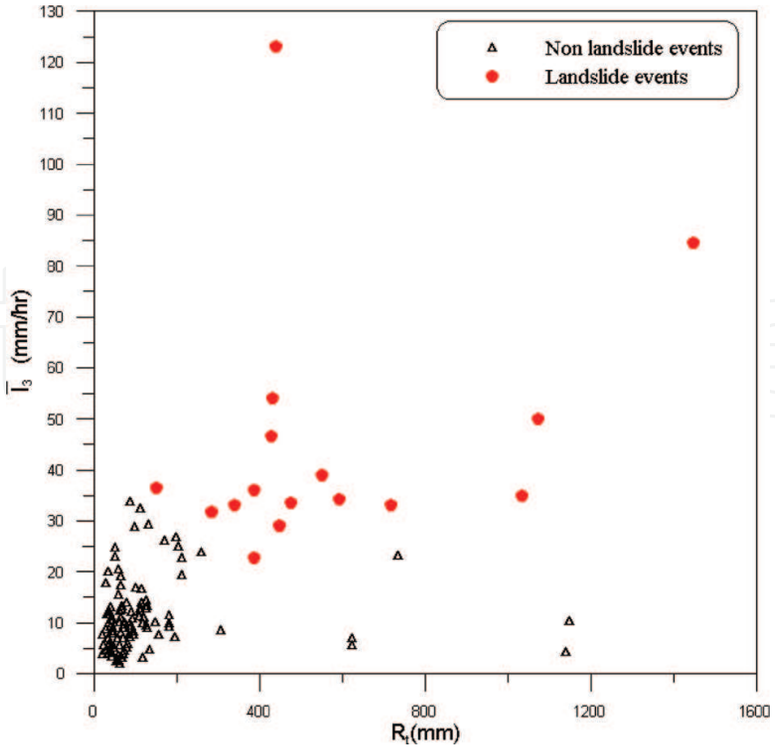


**Figure 20.** Effective accumulative rainfall ($R_t$) against 3-hour average rainfall intensity ($\bar{I}_3$) illustrated from hourly rainfall data recorded by Shinfa gauge.

mitigation and the above mentioned works, Jan [41] has proposed a rainfall-threshold index for landslide mitigation as follow:

$$LRTI = \bar{I}_3 \times R_t \tag{11}$$

where *LRTI* is the landslide rainfall triggering index, $R_t$ is the effective accumulative rainfall, and $\bar{I}_3$ is the 3-hour average rainfall intensity. To establish rainfall threshold for evaluating landslide triggering, the Weibull distribution was used to estimate the values of *LRTI* for the cumulative frequencies at 70% and 90%, respectively, for total rainfall events. During typhoon storms, if its corresponding *LRTI* is greater than the value for the cumulative frequency at 70% (denoted by $LRTI_{70}$), the landslide warning system would issue 'yellow' warning; if the *LRTI* value is greater than the value for the cumulative frequency at 90% (denoted by $LRTI_{90}$), the landslide warning system would issue 'red' warning, as reported by Jan [41]. On the basis of those two LRTI values (at 70 and 90% of cumulative frequency), the operation of landslide warning issuance is suggested following the criterion as

- Level 2 warning would be released when the values of real rainfall data gauging is higher than $LRTI_{70}$.
- Level 1 warning would be released when the values of real rainfall data gauging during a 3-hour period is simultaneously higher than $LRTI_{70}$.
- Level 1 warning would be reduced to Level 2 when the values of real rainfall data gauging during a 3-hour period is simultaneously lower than $LRTI_{70}$.
- Level 2 warning would be left when the values of real rainfall data gauging during a 3-hour period is simultaneously lower than $LRTI_{70}$.

This rainfall-induced, shallow landslide warning system is used to provide information on the decision making of landslide hazard mitigation for Soil and Water Conservation Bureau of Taiwan.

## 5. Conclusions

Severe typhoon storms and the consequent landslide hazards on hillslopes have frequently posed threats to economic implementation whose impacts on the wealth and property may exhaust the available resources to deal with the aftermath of those disasters. In Taiwan, the countermeasures of debris flow have been well developed in recent 20 years, gradually. However, the development of shallow landslide mitigation measures and warning systems are still limited and should be emergent in the future. Moreover, it must need to strengthen public awareness of landslide hazards, educating people on how to respond to landslide hazards on hillsides, especially during rainy seasons. Meanwhile, more research on landslide mechanics, warning system, and its corresponding rationale prediction and assessment methods are necessary.

Occurrence of landslides on hillslopes is not only a real challenge of natural hazard mitigation, but also river channel management. As we above mentioned, ambient Typhoon Morakot had led to significant sedimentation in the Cishan River and the dredging of river channels therefore becomes an important issue after the typhoon disturbance on landscapes. Landslide triggering can simultaneously influence the evolution of hillslope and fluvial systems, leading to its regulation should be integrated and consistent. Hence, Compound-disaster perspective and its domino effect on each disaster are necessary to be considered in the development of landslide countermeasures. In addition, for disaster evaluation in the case of emergency, satellite images, aerial photography and field survey immediate after typhoon storms are necessary to construct high resolution digital topography models that can be used in the aftermath analysis and modeling. Also, more fruitful research on the understanding of landslide mechanics, from which we can develop appropriate design codes in building and installing sediment-control structures, are pressingly needed in Taiwan.

## Acknowledgements

This work was supported by the Ministry of Science and Technology in Taiwan under the Grant No. MOST 104-2221-E-006 -053 -MY3 and MOST 106-2625-M-006-018 -. The writers sincerely appreciate the help of Y.C Wang in digitalizing the widths of the Cishan River.

## Author details

Ssu-Yao Yang[1,2]*, Chyan-Deng Jan[1] and Ji-Shang Wang[3]

*Address all correspondence to: henry740913@gmail.com

1 Department of Hydraulic and Ocean Engineering, National Cheng Kung University, Tainan, Taiwan

2 USDA-ARS National Soil Erosion Research Lab, Purdue University, West Lafayette, IN, USA

3 Ecological Soil and Water Conservation Research Center, National Cheng Kung University, Tainan, Taiwan

## References

[1] Keefer DK. The importance of earthquake-induced landslides to long-term slope erosion and slope-failure hazards in seismically active regions. Geomorphology. 1994;**10**:265-284

[2] Guzzetti F, Ardizzone F, Cardinali M, Rossi M, Valigi D. Landslide volumes and landslide mobilization rates in Umbria, Central Italy. Earth and Planetary Science Letters. 2009;**279**:222-229

[3] Collins BD, Znidarcic D. Stability analyses of rainfall induced landslides. Journal of Geotechnical and Geoenvironmental Engineering. 2004;**130**(4):362-372

[4] Sivrikaya O, Kilic AM, Yalcin MG, Aykamis AS, Sonmez M. The 2001 Adana landslide and its destructive effects, Turkey. Environmental Geology. 2008;**54**:1489-1500

[5] Jan CD, Chen CL. Debris flow caused by typhoon herb in Taiwan. In: Jakob M, Hunger O, editors. Debris-Flow Hazards and Related Phenomena. Berlin: Springer; 2005. pp. 539-563

[6] Dadson SJ, Hovius N, Chen HG, Dade WB, Hsieh ML, Willett SD, Hu JC, Horng MJ, Chen MC, Stark CP, Lague D, Lin JC. Links between erosion, runoff variability and seismicity in the Taiwan orogen. Nature. 2003;**426**:648-651

[7] Kuo CY, Tai YC, Chen CC, Chang KJ, Siau AY, Dong JJ, Han RH, Shimamoto T, Lee CT. The landslide stage of the Hsiaolin catastrophe: Simulation and validation. Journal of Geophysical Research. 2011;**116**:F04007. DOI: 10.1029/2010JF001921

[8] Tsou CY, Feng ZY, Chigira M. Catastrophic landslide induced by typhoon Morakot, Shiaolin, Taiwan. Geomorphology. 2011;**127**:166-178

[9] Central Geological Survey. Query system of environmental geological hazard; 2010. Available at http://envgeo.moeacgs.gov.tw/ (in Chinese)

[10] Dong JJ, Li YS, Kuo CY, Sung RT, Li MH, Lee CT, Chen CC, Lee WR. The formation and breach of a short-lived landslide dam at Hsiaolin Village, Taiwan-part I: Post-event reconstruction of dam geometry. Engineering Geology. 2011. DOI: 10.1016/j.enggeo.2011.04.001

[11] Lee SP, Chen YC, Shieh CL, Kuo YS. Using real-time abnormal hydrology observations to identify a river blockage event resulted from a natural dam. Landslides. 2014;**11**:1007-1017. DOI: 10.1007/s10346-013-0441-1

[12] TGRU. Taiwan geomorphological research unit, Department of Geography, National Taiwan University, Taipei. In: Natural Hazards of Taiwan. Taiwan (in Chinese): Taiwan and Council of Agriculture, Taipei; 2001

[13] Deering DW. Rangeland reflectance characteristics measured by aircraft and spacecraft sensors. In: Ph. D. Dissertation, Texas A & M University. College Station, TX; 1978. p. 338

[14] Dai FC, Lee CF. Frequency-volume relation and prediction of rainfall-induced landslides. Engineering Geology. 2001;**59**:253-266

[15] Hovius N, Stark CP, Allen PA. Sediment flux from a mountain belt derived by landslide mapping. Geology. 1997;**25**(3):231-234

[16] Stark CP, Hovius N. The characterization of landslide size-frequency distributions. Geophysical Research Letters. 2001;**28**(6):1091-1094

[17] Ten Brink US, Geist EL, Andrews D. Size distribution of submarine landslides and its implications to tsunami hazard in Puerto Rico. Geophysical Research Letters. 2006; **33**:L11307. DOI: 10.1029/2006GL026125

[18] Jan CD, Yang SY, Su YW, Huang WS. Investigation about rainfall-induced shallow landslides in CYL and TWR watersheds, Taiwan. Environment and Earth Science. 2016;**75**:898. DOI: 10.1007/s12665-015-5215-8

[19] Bak P. How Nature Works: The Science of Self-Organized Criticality. New York: Springer; 1996

[20] Fujii Y. Frequency distribution of landslides caused by heavy rainfall. Journal of the Seismological Society of Japan. 1969;**22**:244-247

[21] Malamud BD, Turcotte DL. Self-organized criticality applied to natural hazards. Natural Hazards. 1999;**20**:93-116

[22] Guzzetti F, Malamud BD, Turcotte DL, Reichenbach P. Power-law correlations of landslide areas in Central Italy. Earth and Planetary Science Letters. 2002;**195**:169-183

[23] Crosta GB, Negro PD, Frattini P. Soil slips and debris flows on terraced slopes. Natural Hazards and Earth System Sciences. 2003;**3**:31-42

[24] Lave J, Burbank D. Denudation processes and rates in the transverse ranges, southern California: Erosional response of a transitional landscape to external and anthropogenic forcing. Journal of Geophysical Research. 2004;**109**:F01006. DOI: 10.1029/2003JF000023

[25] Clarke BA, Burbank DW. Bedrock fracturing, threshold hillslopes, and limits to the magnitude of bedrock landslides. Earth and Planetary Science Letters. 2010;**297**:577-586

[26] Frattini P, Crosta GB. The role of material properties and landscape morphology on landslide size distribution. Earth and Planetary Science Letters. 2013;**361**:310-319

[27] Hergarten S. Landslides, sandpiles, and self-organized criticality. Natural Hazards and Earth System Sciences. 2003;**3**:505-514

[28] Hufschimidt G, Crozier MJ. Evolution of natural risk: Analysing changing landslide hazard in Wellington, Aotearoa/New Zealand. Natural Hazards. 2008;**45**:255-276

[29] Kreibich H, Thieken AH, Petrow T, Mueller M, Merz B. Flood loss reduction of private households due to building precautionary measures-lessons learned from the Elbe flood in August 2002. Natural Hazards and Earth System Sciences. 2005;**25**:117-126

[30] Turcotte DL. Fractals and Chaos in Geology and Geophysics. Cambridge, UK: Cambridge University Press; 1992. p. 221

[31] Mark DM, Aronson PB. Scale-dependent fractal dimensions of topographic surfaces: An empirical investigation with applications in geomorphology and computer mapping. Mathematical Geology. 1984;**16**(7):671-683

[32] Latrubesse EM, Restrepo JD. Sediment yield along the Andes: Continental budget, regional variations, and comparisons with other basins from orogenic mountain belts. Geomorphology. 2014;**216**:225-233

[33] Walling DE, Fang D. Recent trends in the suspended sediment loads of the world's rivers. Global and Planetary Change. 2003;**39**:111-126

[34] Water Resources Planning Institute. Report on river planning of Chi-San River. In: Water Resources Agency. 2011

[35] Bagnold RA. An approach to the sediment transport problem from general physics. U.S. In: Geological Survey Professional Paper 422-J. 1966

[36] Berti M, Simoni A. Field evidence of pore pressure diffusion in clayey soils prone to landsliding. Journal of Geophysical Research. 2010;**115**:F03031. DOI: 10.1029/2009JF001463

[37] Iverson RM. Sensitivity of stability analyses to groundwater data. In: Bell, editor. Landslides. Balkema, Rotterdam; 1991. pp. 451-457

[38] Caine N. The rainfall intensity–duration control of shallow landslides and debris flows. Geograf Annal. 1980;**62A**:23-27

[39] Tatard L, Grasso JR, Helmstetter A, Garambois S. Characterization and comparison of landslide triggering in different tectonic and climatic settings. Journal of Geophysical Research. 2010;**115**:F04040. DOI: 10.1029/2009JF001624

[40] Wieczorek GF. Effect of rainfall intensity and duration on debris flows in Central Santa Cruz Mountains, California. In: Costa W, editor. Debris Flows/Avalanches: Processes, Recognition and Mitigation. Reviews in Engineering Geology 7. Geological Society of America. 1987. pp. 23-104

[41] Jan CD. A study on the warning system for rainfall-induced sediment disasters. Research Report (SWCB-106-118), Submitted to the Soil and Water Soil Conservation Bureau, Taiwan (in Chinese); 2017

[42] Central Geological Survey. Research on application of the investigation results for the upstream watershed of flood-prone area. In: Central Geological Survey. Chinese: MOEA; 2009

[43] Dadson SJ, Hovius N, Chen H, Dade WB, Lin JC, Hsu ML, Lin CW, Horng MJ, Chen TC, Milliman J, Stark CP. Earthquake-triggered increase in sediment delivery from an active mountain belt. Geology. 2004;**32**:733-736

[44] Feng ZY. The seismic signatures of the surge wave from the 2009Xiaolin landslide-dam breach in Taiwan. Hydrological Processes. 2012;**26**:1342-1351

[45] Chen CY, Yu FC, Lin SC, Cheung KW. Discussion of Landslide Self-Organized Criticality and the Initiation of Debris Flow, Earth Surf. Process. Landforms; 2007;**32**:197-209

[46] Stark CP, Guzzetti F. Landslide rupture and the probability distribution of mobilized debris volumes. Journal of Geophysical Research. 114, F00A02. 2009. DOI: 10.1029/2008JF001008

[47] Wilson JP, Gallant JC. Digital terrain analysis. In: Wilson JP, Gallant JC, editors. Terrain Analysis: Principles and Applications. New York: John Wiley; 2000:1-27

IntechOpen